Theoretical Study of Dual-Function Sensor for Analysis of Blood Composition and Glucose Concentration Based on Nonreciprocal Analog of the Electromagnetically Induced Absorption

Bao-Fei Wan[ID], Bing-Xiang Li[ID], and Hai-Feng Zhang[ID]

Abstract— A nonreciprocal biosensor for the detection of different liquid substances is proposed based on an analog of the electromagnetically induced absorption (EIA-like) effect. Different bright-mode and dark-mode coupling structures are designed for the forward and backward incidences, respectively, and as a result, the incisive EIA-like peaks are staggered at different frequency points. The regulation of nonreciprocal EIA-like effects by the shifts of metal thickness and incident angle is discussed. The EIA-like peaks in different directions occupy different measurement ranges (MRs) and detection capabilities, so they are suitable for detecting blood components and glucose concentrations, accordingly. Multiple layers of analyte cavities are introduced to increase the sensitivity (S) of the sensor. For the forward incidence, the S of the measurement after fitting the response frequency points under different blood components is 190.85 THz/RIU, the figure of merit (FOM) is 367.02, and the detection limit (DL) is 1.36×10^{-4}. For the detection of glucose solution concentration of 0–350 g/L at the backward incidence, the corresponding indicators are 337.46 THz/RIU, 1297, and 3.85×10^{-5} (0.32 g/L). The interferences of the thickness error of the analyte cavity on the sensor are also explored.

Index Terms— Blood components, dual function, electromagnetically induced absorption (EIA-like) effect, glucose solution concentration, nonreciprocal biosensor.

I. INTRODUCTION

BLOOD is an important part of the human body and undertakes many key features such as transporting oxygen, transporting nutrients, and defending against diseases [1], [2], [3]. Blood is composed of plasma, white blood cells, red blood cells, hemoglobin, glucose, and other substances. The lack or excess of any substance will seriously affect the health of the human body. Therefore, blood health is also an important criterion for detecting various diseases, such as leukemia, anemia, lymphoma, and malaria. Thousands of people all over the world die of these diseases every year. Therefore, timely and accurate blood information is very urgent to save lives. Nonetheless, various measurement techniques such as combo test, blood smear, and blood cell count are available, but these methods usually require bulky test environments, complex procedures, or time-consuming [4], [5]. The rise of optical biosensing offers a reasonable option to overcome the traditional shortcomings [6], [7], [8], [9]. By detecting the refractive index information of each blood component, the qualitative and quantitative analysis of blood components or blood sugar concentration can be accurately performed, and the response speed is fast and the structure is compact.

The main optical biometric methods are fluorescence detection and label-free detection [10], [11], [12], [13]. Since the former is challenging to measure many different substances simultaneously, label-free detection is more applicable. With the help of this technology, predecessors have designed several different detection structures using the refractive index properties of different biological indicators. Maji et al. [14] proposed a self-referencing sensor coupled with mixed-mode Tamm plasmon polariton based on two different metallic Bragg mirrors to detect different blood components. The measurement range (MR) of the sensor belongs to 1.33–1.4; the sensitivity (S) is 200 nm/RIU. Panda and Pukhrambam [15] presented a defective 1-D photonic crystals structure for the detection of various elements present in a class of human blood such as plasma, red blood cells, biotin, and serum albumin. The structure adopts CaF_2, $PtSe_2$, and $ZnSe$ as periodic alternating structures, and the walls of defect layers are, respectively, coated with novel 2-D materials, such as WS_2, MoS_2, and graphene, to enhance the sensor performance. The proposed new defect mode sensor achieves an MR of 1.33–1.47 and a maximum S of 1100 nm/RIU. Vafapour et al. [16] tried an optically tunable perfect light absorber as a refractive index metamaterial nanobiosensor, designed to judge chemicals, detect the concentration of water-soluble glucose, and diagnose viruses. The MR and S of water-soluble glucose concentrations are 1.34–1.45 and 300 nm/RIU, respectively.

It should be emphasized that the determination of blood components and the measurement of blood glucose concentration are carried out at the same time in many cases. However, most of the previous studies designed them into two different structures for detection. On the one hand, the

traditional detection technology will increase the capacity of the test sample; on the other hand, different structures will also have different degrees of detection errors. Since the two different analysis samples have different requirements for the MR and the resolving power of the sensor, the research that integrates the two functions has not been significantly improved.

The electromagnetically induced absorption (EIA) effect is first proposed in the laser-driven three-atomic energy-level system [17], [18], [19], [20]. It has attracted the attention of scholars due to its unique dispersion regulatory characteristics in the absorption window. Due to the harsh experimental environmental and experimental conditions, it has severely restricted its application [21], [22]. Fortunately, the researchers later found that in some optical oscillators, these unique dispersion regulation characteristics can also be realized. Despite this, the implementation conditions are much simpler, so it is also called an EIA-like phenomenon [23], [24]. The EIA-like effect is formed by the destructive interference between the phases between different channels and can be formed by the coupling of bright membranes and dark molds. EIA-like effects are usually studied in metasurface structures, but due to the inherent characteristics of 3-D structures, the obtained absorption peaks are too wide to be used for biosensing. If the EIA effect is introduced into the multilayer structure, the absorption peak will become extremely sharp, which will be beneficial for the design of biosensors. However, the relevant reports are very rare to date.

In this article, the silver layer is constructed as a bright model, and the layered periodic structure is set to a dark mold. The resonance effect between the two structures has stimulated the EIA-like effect with high-quality factors. The incident angle and the thickness of the silver layer will affect the nature of bright and dark modes, contributing to the offset of the absorption peak will occur. To meet the requirements of different accuracies for blood composition and glucose concentration, nonreciprocal EIA-like action characteristics are introduced. It should be noted that for the measurement of blood glucose concentration, glucose aqueous solution is substituted for verification in this article. This is mainly because the refractive index of blood glucose concentration is relatively close to that of aqueous glucose solution, and many previous studies have also adopted this alternative method [25], [26].

II. THEORETICAL SENSOR MODEL AND EIA-LIKE EFFECTS

Fig. 1 is the model prototype of the EIA-like phenomenon that is considered. The overall structure is composed of layered cell units Ag, Si, and analyte, and the sequence is Ag_1–$(Si$–$Analyte)^7$–Ag_2.

The thickness of the Si layer is $d_{si} = 90$ nm, and the refractive index of silicon is expressed as [27], as in (1), shown at the bottom of the next page.

The thickness of the Ag film is $d_{m1} = d_{m2} = 60$ nm. The dielectric function of Ag is illustrated by [28]

$$\varepsilon_r = \varepsilon_\infty - \frac{\omega_p^2}{\omega^2 + i\omega\gamma} - \frac{\Delta\Omega^2}{(\omega^2 - \Omega^2) + i\Gamma} \tag{2}$$
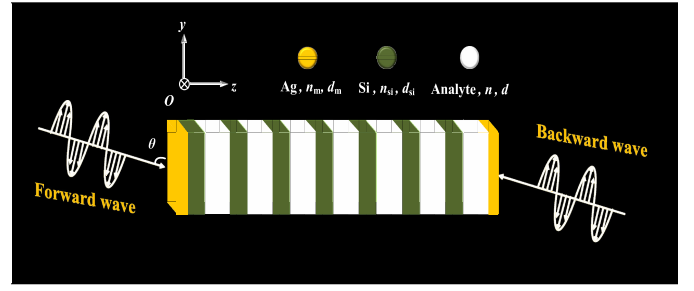

Fig. 1. Proposed structure diagram of the nonreciprocal EIA-like effect. The structure is composed of metal silver, medium Si, and analyte alternately, and the component is Ag_1–$(Si$–$Analyte)^7$–Ag_2. For the forward incidence, Ag_1 and $(Si$–$Analyte)^7$–Ag_2 are defined as structures 1 and 2, respectively. For the backward incidence, Ag_2 and $(Analyte$-$Si)^7$–Ag_1 are correspondingly understood as structures 3 and 4.

where $\omega = 2\pi f$ is the angular frequency and f represents the frequency. $\varepsilon_\infty = 2.4064$, $\Omega_p = 2\pi \times 2214.6 \times 10^{12}$ Hz, $\gamma = 2\pi \times 4.8 \times 10^{12}$ Hz, $\Delta = 1.6604$, $\Omega = 2\pi \times 1330.1 \times 10^{12}$ Hz, and $\Gamma = 2\pi \times 620.7 \times 10^{12}$ [28].

The thickness of the analyte is $d = 450$ nm, and the refractive index is determined by the specific object to be measured. However, it is given a value of 1.36 for theoretical interpretation in the early stage.

The energy communication between layers is described by the transfer matrix method [28]

$$M_i = \begin{bmatrix} \cos\delta_i & -jp_i^{-1}\sin\delta_i \\ -jp_i\sin\delta_i & \cos\delta_i \end{bmatrix}. \tag{3}$$

Among them, $\delta_i = (2\pi/\lambda)n_i d_i \cos\theta_i$, where $\lambda = 2\pi c/\omega$ and $p_i = (\varepsilon_0/\mu_0)^{1/2}n_i \cos\theta_i$(TE wave). θ_i indicates the propagation angle within the ith layer, and its original value is 30°.

The reflection coefficient r and transmission coefficient t can be described by the following formulas:

$$r = \left| \frac{(M_{11} + M_{12}p_0)p_0 - (M_{21} + M_{22}p_0)}{(M_{11} + M_{12}p_0)p_0 + (M_{21} + M_{22}p_0)} \right| \tag{4}$$

$$t = \left| \frac{2p_0}{(M_{11} + M_{12}p_0)p_0 + (M_{21} + M_{22}p_0)} \right|. \tag{5}$$

The reflectivity R and transmittance T are presented as

$$\begin{aligned} R &= |r|^2 \\ T &= |t|^2. \end{aligned} \tag{6}$$

The absorptivity A can be expressed as

$$A = 1 - |r|^2 - |t|^2. \tag{7}$$

The S value, figure of merit (FOM), and detection limit (DL) are important parameters to evaluate a sensor, and an excellent sensor corresponds to a higher S, a higher FOM, and a lower DL [27]. Corresponding definitions can be expressed as follows, where Δf and Δn refer to the frequency and refractive index change, while f_T symbolizes the resonant frequency, and FWHM implies the full-width at half-maxima

of the resonant peak [27]

$$\text{Sensitivity} = \frac{\Delta f}{\Delta n} \quad (8)$$

$$\text{FOM} = \frac{S}{\text{FWHM}} \quad (9)$$

$$\text{DL} = \frac{f_T}{20SQ}. \quad (10)$$

The EIA-like effect is caused by phase destructive interference between two different channels, and absorption characteristics will occur when phase difference meets the conditions for interference enhancement. Bright resonators can be directly coupled to external energy, while dark resonators fail to possess this ability. The bright resonator first couples energy from the outside and transmits it to the dark resonator, which then transfers energy to the bright resonator, simulating the two-channel transition process in a three-level atomic system that excites the EIA-like properties.

To explain EIA-like characteristics more forcefully, the two-oscillator model is introduced. If the bright resonator and the dark resonator represent oscillators 1 and 2, respectively, the following relationship will be satisfied [29]:

$$\ddot{x}_1(t) + \gamma_1 \dot{x}_1(t) + \omega_0^2 x_1(t) + \Omega x_2(t) = g E_0(t)$$
$$\ddot{x}_2(t) + \gamma_2 \dot{x}_2(t) + (\omega_0 + \delta)^2 x_2(t) + \Omega x_1(t) = 0 \quad (11)$$

where x_1 and x_2 stand for resonant amplitudes, while γ_1 and γ_2 indicate resonance damping ($\gamma_2 \ll \gamma_1$). If the bright and dark modes are stimulated by the external electric field, $E_0(t) = E_0 e^{i\omega t}$, and the coupling coefficient is g. δ is the detuning factor, and Ω is regarded as the coupling strength between the two oscillators. The displacement vector $X_n(t) = a_n e^{i\omega t}$ ($n = 1, 2$). The amplitudes of the two modes can be expressed as [29]

$$a_1(\omega) = \frac{-g E_0(\omega^2 + i\omega\gamma_2 - (\omega_0 + \delta)^2)}{(\omega^2 + i\omega\gamma_1 - \omega_0^2)(\omega^2 + i\omega\gamma_2 - (\omega_0 + \delta)^2) - \Omega^2} \quad (12)$$

$$a_2(\omega) = \frac{g E_0 \Omega}{(\omega^2 + i\omega\gamma_1 - \omega_0^2)(\omega^2 + i\omega\gamma_2 - (\omega_0 + \delta)^2) - \Omega^2}. \quad (13)$$

Therefore, the system absorption is obtained by calculating the dissipated energy as follows:

$$A(\omega) = \frac{i g^2 \omega(\omega + i\omega\gamma_2 - \omega^2)}{(\omega^2 + i\omega\gamma_1 - \omega_0^2)(\omega^2 + i\omega\gamma_2 - (\omega_0 + \delta)) - \Omega^2}. \quad (14)$$

With the approximation $\omega_0^2 - \omega^2 \approx -2\omega_0(\omega - \omega_0)$, (14) can be simplified as [29]

$$A(\omega) = \text{Re}\left(\frac{i g^2 (\omega - (\omega_0 + \delta) + i\gamma_2/2)}{(\omega - \omega_0 + i\gamma_1/2)(\omega - (\omega_0 + \delta) + i\gamma_2/2) - \Omega^2/4}\right). \quad (15)$$

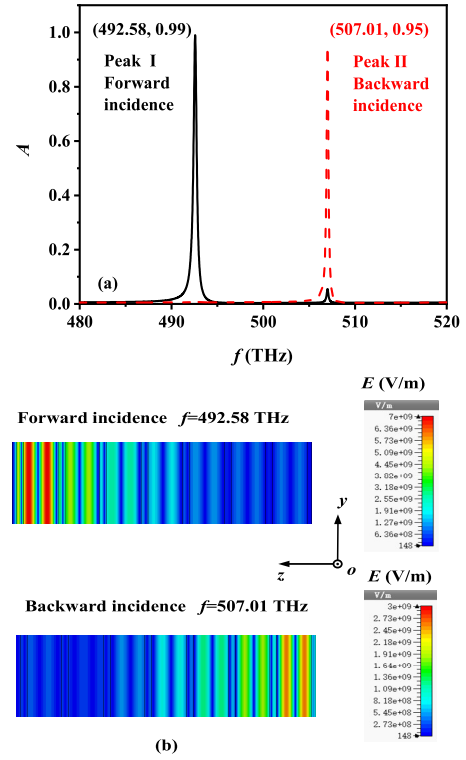The Re( ) function refers to taking the real part.

Fig. 2. (a) Absorption peaks excited by the electromagnetic waves incident from the opposite direction. (b) Electric field energy distribution at frequency point of absorption peaks.

III. ANALYSIS AND DISCUSSION

A. Verification of EIA-Like Effects

For the convenience of theoretical explanation, Ag_1 and $(Si–Analyte)^7–Ag_2$ are classified as structures 1 and 2, respectively, while Ag_2 and $(Analyte-Si)^7–Ag_1$ are referred to as structures 3 and 4, respectively. In Fig. 2(a), when the electromagnetic wave is incident forward, an EIA-like peak I with an absorptivity of 0.99 appears at the position of 492.58 THz. In the case of the backward incidence, the EIA-like peak II with an absorptivity of 0.95 occurs at 507.01 THz. The distribution of electric field capacity in Fig. 2(b) shows this process more clearly. For the forward wave, the high electric field energy is only distributed near the junction of structure 1 and structure 2, which means that the electromagnetic wave can only propagate to this point and then be absorbed, suggesting the phenomenon of high absorption. On the contrary, if the electromagnetic wave can be completely transmitted through the structure, then the whole structure will be distributed with energy. Similarly, for backward incidence, the energy of the electromagnetic wave is also only distributed at the junction of structures 3 and 4, rather than throughout the whole structure, which indicates the strong absorption characteristic at this frequency point. This is mainly because the Ag_1 layer is in close contact with the medium Si, while the Ag_2 layer is connected with the object to be measured. The refractive

$$n_{si} = \sqrt{\left(1 + \frac{10.6684293\,\lambda^2}{\lambda^2 - 0.301516485^2} + \frac{0.0030434748\,\lambda^2}{\lambda^2 - 1.13475115^2} + \frac{1.54133408\,\lambda^2}{\lambda^2 - 1104^2}\right)} \quad (1)$$

indexes of the medium Si and the analyte are obviously different, and the electric field energy is mainly concentrated at the interface between the metal layer and other layered structures, so the refractive index of the medium in closest contact with the metal is mainly responsible for the position of the absorption peak.

In Fig. 3, both the bright-dark mode coupling theory and the two-oscillator model are referenced concurrently for a more in-depth elaboration. In Fig. 3(a), structure 1 takes possession of a certain absorption performance, so it can be regarded as a bright resonator, while structure 2 has a few absorption performances and can be understood as a dark resonator. After the combination of the two structures, the structure 1 couples the energy obtained from the outside to structure 2, which then transfers the energy to structure 1, thus triggering a strong EIA-like phenomenon at 492.58 THz. In Fig. 3(b), the simulation results are compared with the calculated results of the two-oscillator model, and their fitting degree is in line with the conditions. The fitting variables are $\gamma_1 = 3.4$ THz, $\gamma_2 = 1.5$ GHz, $\omega_0 = 492.58$ THz, $\delta = 15$ GHz, $\Omega = 0.75$ GHz, and $g = 1.36$ MHz. In Fig. 3(c), structure 3 has a certain absorption capacity when excited alone, while the structure 4 absorbs very little energy when excited alone, so the two are considered to be bright resonators and dark resonators accordingly. The external energy is first coupled by structure 3, which diffuses part of the energy to structure 4, which in turn transfers the energy to structure 3, thus forming a drastic absorption phenomenon at 507.01 THz. In Fig. 3(d), the simulation results and the simulation circumstances are also apropos. The simulation parameters are $\gamma_1 = 2$ THz, $\gamma_2 = 1.5$ GHz, $\omega_0 = 507.01$ THz, $\delta = 15$ GHz, $\Omega = 0.75$ GHz, and $g = 0.76$ MHz.

The three-level atomic transition system is also productive for the formation of EIA-like phenomena. In Fig. 4(a), under the case of the forward wave, the process of energy level transition and the coupling process of the bright and dark modes are described simultaneously, including ground state $|0\rangle$, metastable state $|2\rangle$, and excited state $|1\rangle$. Ω_c and Ω_p demonstrate the frequency conditions that need to be met to produce the transition, and γ_c and γ_p represent the coupling coefficients between the energy levels. In the three-level system, the excitation of pump light makes the transition between $|0\rangle$ and $|1\rangle$ open, while the introduction of probe light forces the transition between $|1\rangle$ and $|2\rangle$. Similarly, in the proposed structure, the $|0\rangle-|1\rangle$ transition pathway is generated only when structure 1 (bright resonator) is operating, while the introduction of structure 2 (dark resonator) promotes another transition pathway of $|1\rangle-|2\rangle$. When the two transition channels produce destructive interference and the condition of enhanced phase interference is satisfied, a new absorption window will be excited. In Fig. 4(b), the transition process is similar in the case of backward incidence, except that structures 3 (bright resonator) and 4 (dark resonator) replace the role of pump light and probe light, respectively.

B. Effects of Incident Angle and Metal Thickness

In Fig. 5, the impacts of incident angle and metal thickness on the EIA-like effects are considered. In Fig. 5(a),
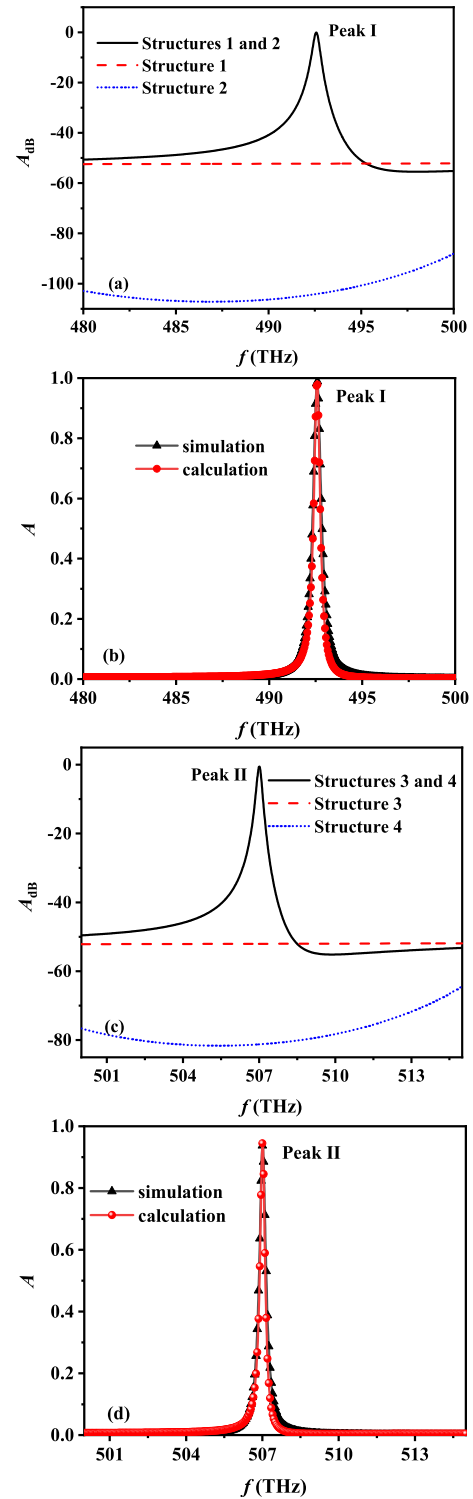

Fig. 3. In the case of forward incidence: (a) coupling effect of the bright and dark modes between structure 1 and structure 2 and (b) simulation results of dual-oscillator model and the original simulation results. In the case of backward incidence: (c) coupling effect of the bright and dark modes between structure 3 and structure 4 and (d) simulation results of dual-oscillator model and the original simulation results.

multiple absorption peaks appear over a wide frequency range. However, because the other peaks do not meet the formation conditions of the EIA-like effect, it is considered that they are generated by the cavity resonance of periodic structure,
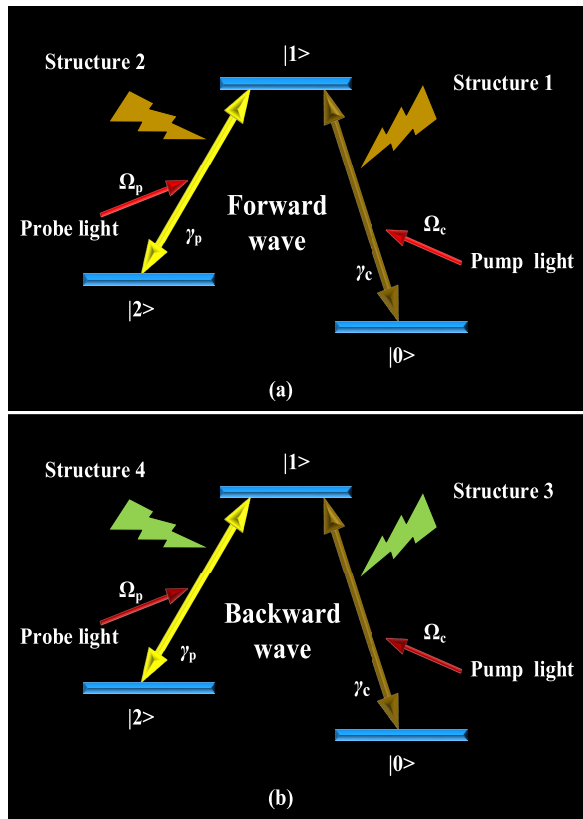
Fig. 4. Classical energy level transition theory of EIA-like effect under (a) forward wave and (b) backward wave.

Fig. 5. Impacts of (a) incident angle θ, (b) thickness of Ag$_1$ layer d_{m1}, and (c) thickness of Ag$_2$ layer d_{m2} on EIA-like performances.

which is not in the scope of discussion. With the increase of θ, peak I and peak II move toward the high-frequency direction, and the frequency difference between peaks gradually expands. Compared with the small θ value, the larger θ is conducive to the improvement of absorption capacity. In Fig. 5(b), with the expansion of d_{m1}, peak I moves toward the high frequency, while the frequency position of peak II fails to shift, and the thickness of the metal significantly affects the intensity of peak I. When d_{m1} is 50 or 70 nm, the EIA-like peak I is higher than 0.9. In addition, the absorption capacity deteriorates significantly. In Fig. 5(c), controlling the distribution of d_{m2} only affects one EIA-like peak. With the expansion of the thickness, the peak II moves to the high-frequency direction, but the frequency position of the peak I does not adjust. If d_{m2} is equal to 50 or 70 nm, peak II still maintains a high level above 0.9, but if the thickness exceeds this range, the absorption capacity decreases significantly. It can be observed that since Ag$_1$ layer acts as the bright mode when the electromagnetic wave is forward incident, and Ag$_2$ layer serves as the bright mode under the backward incidence, the alteration in thickness will only independently affect the respective absorption peaks.

The artificial formula for N is used to emphasize the nonreciprocal absorption property, which is numerically equivalent to the absolute value of the difference between the forward and backward absorptivity.

$$N = |A_{\text{forward}} - A_{\text{backward}}|. \tag{16}$$

The adjustment of θ can affect the energy coupling degree of both the bright resonator and the dark resonator, so the
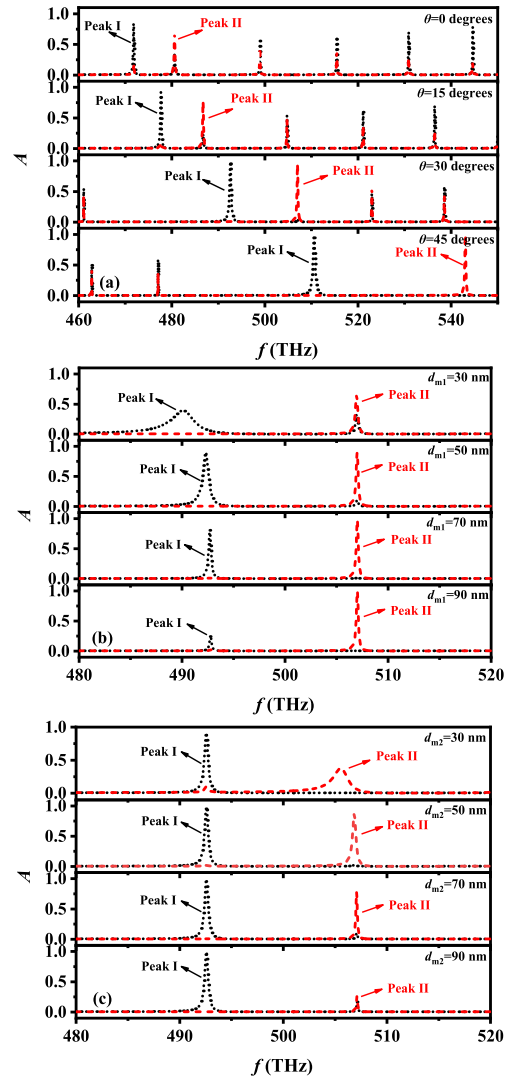
regulating function of θ change on the nonreciprocal EIA-like effect will be obvious. In Fig. 6(a), as θ expands from 0° to 40°, both forward-incident peak I and backward-incident peak II will produce a blue shift effect, and peak II moves faster. Meanwhile, N values are very conspicuous in the process of migration. Metal Ag is a high-loss medium and plays the role of a bright resonator, so its thickness variation also significantly affects the performance of the nonreciprocal EIA-like effect. In Fig. 6(b), when d_{m1} increases from 30 to 80 nm, the nonreciprocity of peak I generally shows an upward trend, while the regulation of peak II is not distinct. In Fig. 6(c), if d_{m2} shifts from 30 to 80 nm, the phenomenon is just the opposite, with peak I increasing while peak II almost keeping the original state. It can be understood that the extension of the thickness of the metal layer provides more favorable conditions for the sufficient reaction between the electromagnetic wave and the internal particles of the metal.

C. Analysis of Sensing Performance and Interference Study

As can be seen from Fig. 2(a), the emerging nonreciprocal EIA-like peak not only has a strong absorptivity but also has
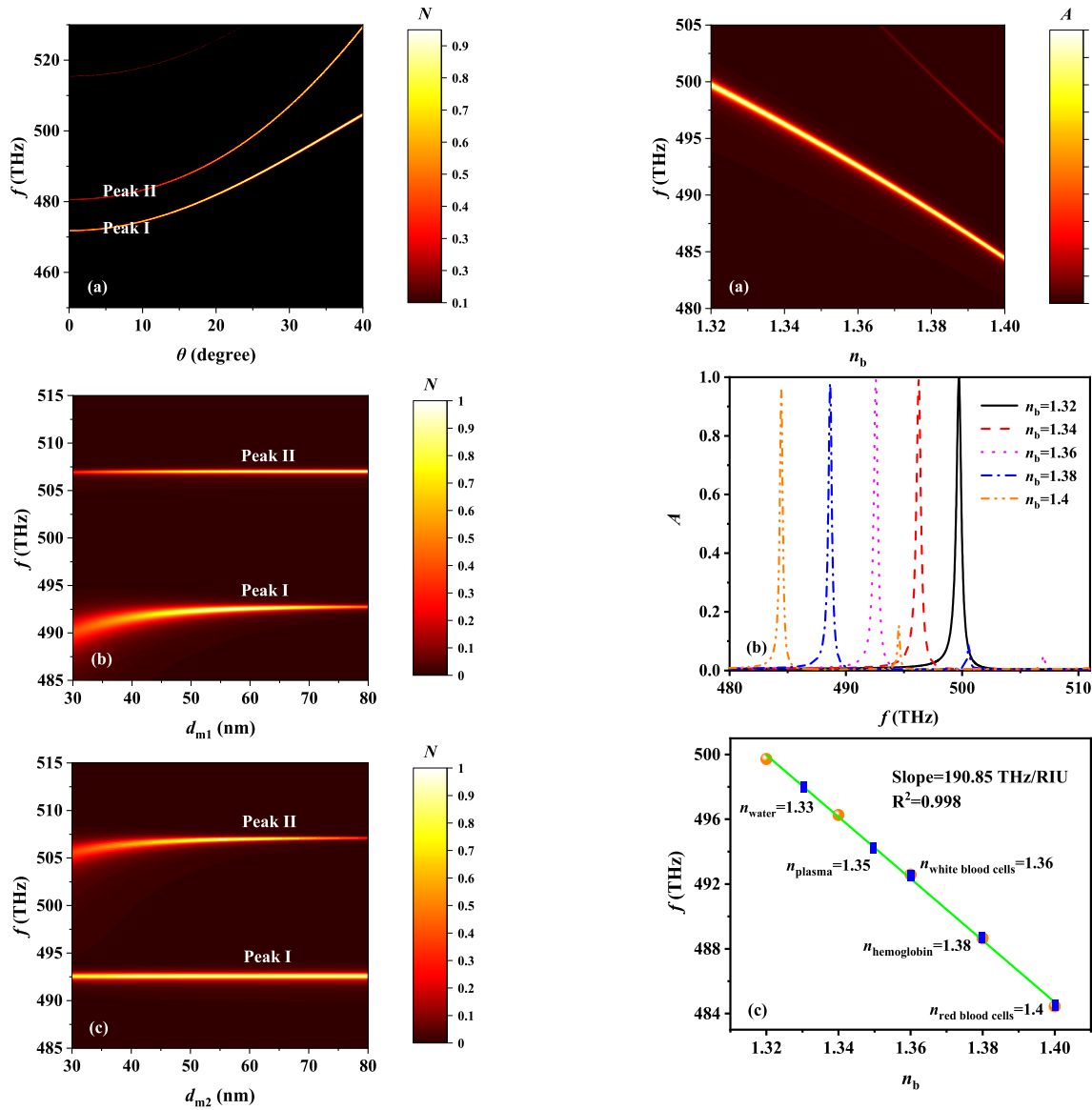
Fig. 6. Impacts of (a) incident angle θ, (b) thickness of Ag$_1$ layer d_{m1}, and (c) thickness of Ag$_2$ layer d_{m2} on nonreciprocal EIA-like performances.
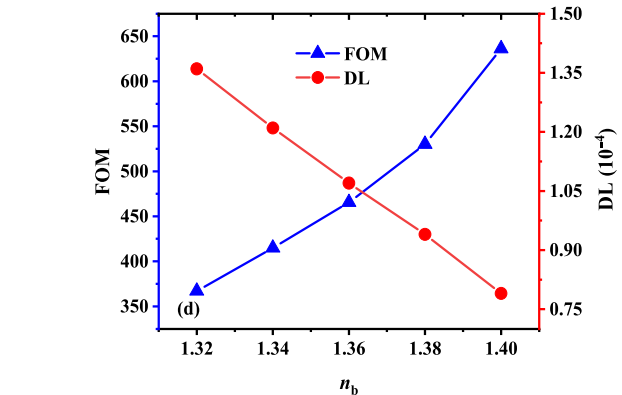

Fig. 7. In the case of blood composition detection under forward incidence: (a) variation of EIA-like peak positions with refractive indexes, (b) EIA-like phenomena with refractive indexes of 1.1, 1.2, 1.3, 1.4, and 1.5, respectively, (c) linear fit of analyte resonance frequencies, and (d) FOM and DL distribution of analytes.

a narrow FWHM, which occupies the potential to be used as a sensor. In Fig. 7(a), when incident light propagates forward, the refractive index of n_b falls within the range of 1.32–1.4, and the frequency shift of the EIA-like peak point also occurs as a linear redshift. In Fig. 7(b), when n_b values are 1.32, 1.34, 1.36, 1.38, and 1.4, respectively, the corresponding resonant frequency points are 499.72, 496.26, 492.58, 488.65, and 484.44 THz, and the FWHM values are 0.52, 0.46, 0.41, 0.36, and 0.3 nm. In Fig. 7(c), the variation of resonance frequency point and n_b are fit, and the fitting degree R^2 is 0.998. The water ($n_{water} = 1.33$), plasma ($n_{plasma} = 1.33$), white blood cells ($n_{whitebloodcells} = 1.33$), hemoglobin ($n_{hemoglobin} = 1.33$), and red blood cells ($n_{redbloodcells} = 1.33$) in the blood group ingredients happen to fall within the MR, and the S is as high as 190.85 THz/RIU. In Fig. 7(d), with the refractive index distribution, the FOM presents the rule of rise, taking the values 367.02, 414.89, 465.48, 530.14, and 636.17 in order. Conversely, DL shows a trend of decline, and the

corresponding indicators are, respectively, 1.36×10^{-4}, 1.21×10^{-4}, 1.07×10^{-4}, 9.4×10^{-5}, and 7.9×10^{-5}.

For the sensor, considering the possible errors, the analytical layer will have potential deviations when filling, so the weak
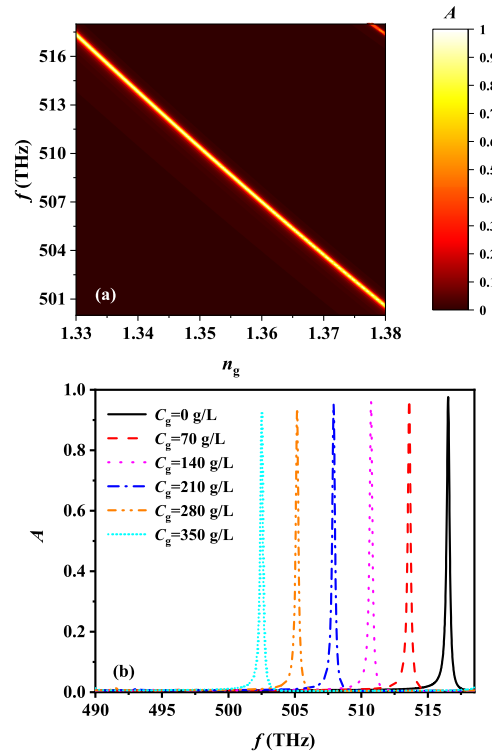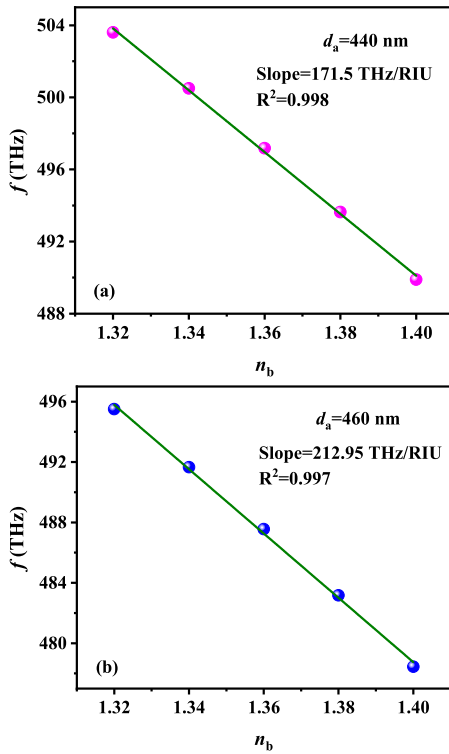
Fig. 8. Regulation of blood composition detection when the thicknesses of analyte layer are (a) 440 nm and (b) 460 nm, respectively.

changes of d_a are also taken into account. In Fig. 8(a), when the value of d_a is lower than the original value of 10 nm, it is also in the case of 440 nm, the MR is 1.32–1.4, the R^2 value is 0.998, the S is 171.5 THz/RIU, and the various blood components that are originally measured are included. In Fig. 8(b), if the value of d_a is higher than the original value of 10 nm, that is, 450 nm, the MR is still 1.32–1.4, which contains the blood component that needs to be measured, and the R^2 value is 0.997, and S is 212.95 THz/RIU. Relatively speaking, the reduction of d_a is conducive to improving S indicators for the detection of the blood component of the front to an incident.

In Fig. 9(a), if n_g belongs to 1.33–1.38, the peak point of EIA-like maintains an efficient linear relationship with it, which is suitable for the glucose solution concentration C_g detection in the range of 0–350 g/L [26]

$$n_g = 1.33230545 + 0.00011889 C_g. \quad (17)$$

In Fig. 9(b), when C_g rises from 0 to 350 g/L with intervals of 70 g/L, the refractive index aggrandizes from 1.3323 to 1.3739. The corresponding frequency point and FWHM values are 516.53, 513.6, 510.73, 507.92, 505.17, and 502.49 THz, and 0.26, 0.26, 0.25, 0.25, 0.24, and 0.23 nm, respectively. The linear relationship between EIA-like peak points and C_g is fit in Fig. 9(c), and the results exhibit that R^2 is equal to 0.999 and S is 337.46 THz/RIU in the MR of 1.3323–1.3739 (C_g of 0–350 g/L). In Fig. 9(d), with the change of glucose concentration, the FOM values increase, taking the values 1297.92, 1297.92, 1349.84, 1349.84, 1406.08, and 1467.22 in turn. DL exhibits a downward trend, and the corresponding
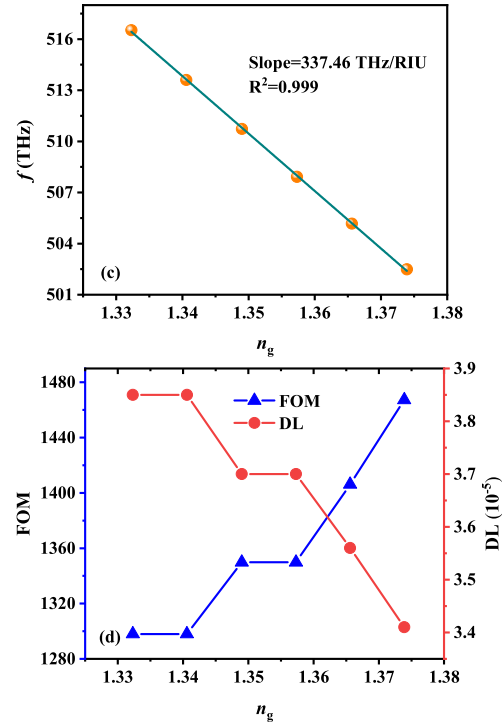
Fig. 9. In the case of glucose aqueous solution detection under backward incidence: (a) variation of EIA-like peak positions with refractive indexes, (b) EIA-like phenomena with glucose concentration of 0, 70, 140, 210, 280, and 350 g/L, respectively, (c) linear fit of analyte resonance frequencies, and (d) FOM and DL distribution of analytes.

indicators are, respectively, 3.85×10^{-5}, 3.85×10^{-5}, 3.7×10^{-5}, 3.7×10^{-5}, 3.56×10^{-5}, and 3.41×10^{-5}.

For glucose solution sensing, the effect of the thickness of the cavity is also analyzed. In Fig. 10(a), when the value of d_a is lower than the original value of 10 nm, it is also in the

Fig. 10. Regulation of glucose aqueous solution detection when the thicknesses of analyte layer are (a) 440 and (b) 460 nm, respectively.
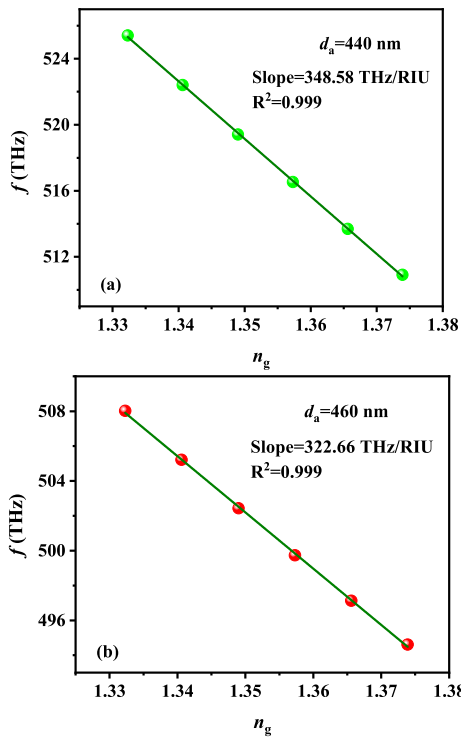
TABLE I
INFLUENCES OF DIFFERENT THICKNESS ERROR COEFFICIENTS ON SENSOR PERFORMANCE

Analyte	β	MR	S (THz/RIU)	DL (10^{-4} RIU)	R^2
Blood composition	0.95	1.32~1.4 RIU	176.9	1.92	0.998
	1	1.32~1.4 RIU	190.85	1.36	0.998
	1.05	1.32~1.4 RIU	202.7	0.986	0.998
Glucose solution	0.95	0~350 g/L	355.21	0.521	0.999
	1	0~350 g/L	337.46	0.385	0.999
	1.05	0~350 g/L	319.71	0.312	0.999

case of 440 nm, the MR is 0–350 g/L, the R^2 value is 0.999, and S is 348.58 THz/RIU. In Fig. 10(b), if the value of d_a is higher than the original value of 10 nm, that is, 460 nm, the MR is still 0–350 g/L, and the R^2 value is 0.999, and the S is 322.46 THz/RIU. Similar to blood composition tests, a decrease in d_a also helps to optimize S.

Interference study is important to validate in the real application. The common interference mainly comes from two parts, one is the dielectric thickness error, and the other is the dielectric loss error.

For the thickness error, with the current technology, a thickness error of less than 5% can be done, so we discuss this. For the convenience of expression, the error coefficient coefficient β is introduced, where β refers to the offset of the thickness of all media in proportion to the original basis. The specific performance analysis is shown in Table I. For blood component detection, with the increase in β, MR is
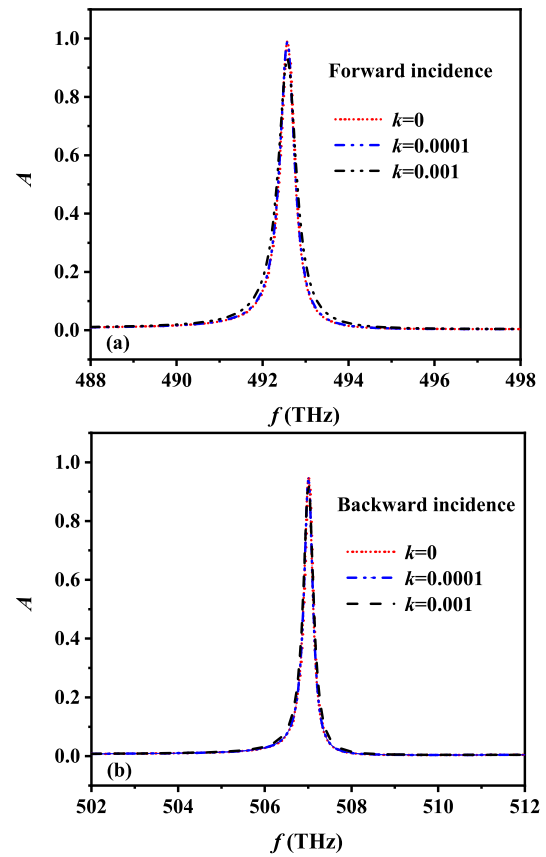

Fig. 11. Effects of extinction coefficient k on absorption peaks excited by (a) forward incident wave and (b) backward incident wave.

not affected and S is gradually increased. DL is reduced, which means that the resolution is enhanced, while the fitting accuracy remains at a high level. For the detection of glucose solution concentration, if β is increased, MR is constant and S decreases. DL is also reduced, but this means that the resolution goes up and the fitting accuracy stays the same. Therefore, the proposed sensor, due to the introduction of uncontrollable thickness errors during the experiment, should be tested after the completion of structural machining. And the final sensing performance is subject to the test results rather than the simple theoretical simulation reference. Theoretical simulation is also necessary because the theoretical results and error results are similar; theoretical simulation can guide sensor design.

In the case of metallic silver, the loss itself is taken into account, so it will not be repeated here. Although the loss of silicon medium is very low, the distribution of several extinction coefficients is discussed here to study the effect of loss on sensor performance. As analyzed in the manuscript, the absorption peak stimulated by the forward wave is used to measure blood composition, and the absorption peak stimulated by the backward wave is used to measure glucose concentration. In Fig. 11(a), for the forward incident electromagnetic wave, that is peak I used to measure blood composition, when the extinction coefficient is 0, 0.0001, 0.001, respectively, the operating frequency and FWHM values are 492.58, 492.58, and 492.58 THz and 0.41°, 0.43°,

TABLE II
COMPARISON OF THIS WORK WITH PREVIOUS STUDIES

Refs.	Year	Principle	Non-reciprocity	Multi-functionality	Blood components		Glucose concentration		
					S	MR	S	MR	DL
[14]	2018	Optical Tamm state	None	None	200 nm/RIU	water, plasma, white blood cells, hemoglobin, red blood cells	None		
[15]	2021	Defect mode	None	None	1100 nm/RIU	water, plasma, red blood cell, biotin, serum albumin	None		
[16]	2021	Metasurface technology	None	None	None		300 nm/RIU	0-600 g/L	5.9×10^{-3} RIU
[25]	2020	Grating	None	None	None		2600 nm/RIU	0-300 g/L	3.79×10^{-5} RIU
[28]	2021	Optical Tamm state	None	Yes	None		2.76 nm/RIU	140-330 g/L	1.5×10^{-4} RIU
This work	2023	EIA-like effect	Yes	Yes	236 nm/RIU	water, plasma, white blood cells, hemoglobin, red blood cells	390 nm/RIU	0-350 g/L	3.85×10^{-5} RIU

0.52°, respectively. In Fig. 11(b), for the backward incident electromagnetic wave, that is peak II used to measure glucose aqueous solution, when the extinction coefficient is 0, 0.0001, 0.001, respectively, the operating frequency and FWHM values are 507.01, 507.01, and 507.01 THz and 0.24°, 0.25°, and 0.29°, respectively. The results show that the enhanced loss has no effect on the location of the resonant frequency, which means that S and MR of the sensor are not affected, either for the detection of blood composition or the concentration of glucose solution. The FWHM values will increase to a certain extent, but this increase is not obvious and will not significantly affect DL, so the impact of loss on the sensor is weak.

To show more clearly the characteristics of the proposed sensor, Table II is designed for performance comparison. Most previous sensor designs focused on improving the performance of single-function sensors, while in this article, a nonreciprocal transmission mode is designed to enable the sensor to detect two different analytes in opposite incident directions, which is an advantage that previous studies do not have.

In addition, manufacturing complexity, cost, and feasibility are compared. The structure of this manuscript belongs to the multilayer structure, and [14], [15], and [28] are multilayer structures, so there is little difference in manufacturing complexity. However, the structures of [16] and [25] are metasurface technology and grating structure, respectively, and the multilayer structure is simpler to process. In terms of cost, because the multilayer structure is easy to process, the cost is relatively lower than that of [16] and [25]. However, the structures in [14] and [15] can only realize the detection of one analyte, and if two analytes are to be detected, two structures need to be processed, so the proposed structure has the advantage in cost. Although the structure in [28] is capable of measuring both analytes, it does not involve blood components. And the sensitivity of its glucose solution concentration sensor is extremely low. As for feasibility, biosensors based on multilayer structures have been studied and reported in large numbers, such as [14], [15], and [28]. Therefore, theoretically speaking, feasibility is available.

IV. CONCLUSION

In general, in this article, nonreciprocal EIA-like effects occur by constructing differentiated bright and dark mode structures in opposite directions. An increase in the incidence angle can extend the frequency difference between peak I and peak II, while the thickness of the metal affects the absorptivity. Peak I is suitable for the detection of water, plasma, white blood cells, hemoglobin, and red blood cells in the blood. The MR, S, FOM, and DL are 1.32–1.4, 190.85 THz/RIU, 367.02, and 1.36×10^{-4}, respectively. Peak II is helpful to determine the concentration of glucose solution, and the corresponding indexes are 1.3323–1.3739 (0–350 g/L), 337.46 THz/RIU, 502.49, and 3.85×10^{-5} (0.32 g/L) respectively. The reduction of analyte layer thickness is beneficial to optimize S of the detected object without weakening the MR.

This article presents a dual-function sensor that can be used to detect blood composition and glucose concentration. It is also a refractive index sensor in essence, so the proposed sensor can also be used to detect other substances with similar refractive index. In addition, the core idea of this article is to extend the MR of the sensor by using the nonreciprocal property. For other categories of sensors, when the MR is insufficient, the same principle can be adopted to expand. Importantly, the current research is still in the theoretical stage, and the most important concern at this stage is to propose novel design schemes theoretically to make up for the shortcomings of traditional sensors. In the future, we will continue the in-depth research and further consider the problems of experimental verification and practical application.

REFERENCES

[1] F. Bănică, *Chemical Sensors and Biosensors: Fundamentals and Applications*. Chichester, U.K.: Wiley, 2012.

[2] M. Calcerrada, C. García-Ruiz, and M. González-Herráez, "Chemical and biochemical sensing applications of microstructured optical fiber-based systems," *Laser Photon. Rev.*, vol. 9, no. 6, pp. 604–627, Nov. 2015.

[3] J. Harris and J. Zehnder, "A compact optical sensor for parallel analysis of blood components," SANOFI-Supported Biostar Sponsored Res. Project, 2011. [Online]. Available: https://biox.stanford.edu/research/seed-grants-biostar-grant-program/compact-optical-sensor-parallel-analysis-blood-components

[4] E. Yablonovitch, "Inhibited spontaneous emission in solid-state physics and electronics," *Phys. Rev. Lett.*, vol. 58, no. 20, pp. 2059–2062, May 1987.

[5] M. O'Toole and D. Diamond, "Absorbance based light emitting diode optical sensors and sensing devices," *Sensors*, vol. 8, no. 4, pp. 2453–2479, Apr. 2008.

[6] G. Morales-Luna, M. Herrera-Domínguez, E. Pisano, A. Balderas-Elizalde, R. I. Hernandez-Aranda, and N. Ornelas-Soto, "Plasmonic biosensor based on an effective medium theory as a simple tool to predict and analyze refractive index changes," *Opt. Laser Technol.*, vol. 131, Nov. 2020, Art. no. 106332.

[7] S. Singh and V. Kaur, "Photonic crystal fiber sensor based on sensing ring for different blood components: Design and analysis," in *Proc. 9th Int. Conf. Ubiquitous Future Netw. (ICUFN)*, Jul. 2017, pp. 399–403.

[8] K. Ahmed et al., "Refractive index-based blood components sensing in terahertz spectrum," *IEEE Sensors J.*, vol. 19, no. 9, pp. 3368–3375, May 2019.

[9] S. Chu, K. Nakkeeran, A. M. Abobaker, S. S. Aphale, P. R. Babu, and K. Senthilnathan, "Design and analysis of surface-plasmon-resonance-based photonic quasi-crystal fiber biosensor for high-refractive-index liquid analytes," *IEEE J. Sel. Topics Quantum Electron.*, vol. 25, no. 2, pp. 1–9, Mar. 2019.

[10] X.-J. Tan and X.-S. Zhu, "Optical fiber sensor based on Bloch surface wave in photonic crystals," *Opt. Exp.*, vol. 24, no. 14, p. 16016, 2016.

[11] H. Abdullah, K. Ahmed, and S. A. Mitu, "Ultrahigh sensitivity refractive index biosensor based on gold coated nano-film photonic crystal fiber," *Results Phys.*, vol. 17, Jun. 2020, Art. no. 103151.

[12] A. A. Revathi and D. Rajeswari, "Surface plasmon resonance biosensor-based dual-core photonic crystal fiber: Design and analysis," *J. Opt.*, vol. 49, no. 2, pp. 163–167, Jun. 2020.

[13] C.-F. Lai and J.-S. Li, "Active visualized solvent sensor based on copolymer hydrogel photonic crystals containing white LEDs," *Sens. Actuators B, Chem.*, vol. 286, pp. 394–400, May 2019.

[14] P. S. Maji, M. K. Shukla, and R. Das, "Blood component detection based on miniaturized self-referenced hybrid Tamm-plasmon-polariton sensor," *Sens. Actuators B, Chem.*, vol. 255, pp. 729–734, Feb. 2018.

[15] A. Panda and P. D. Pukhrambam, "A theoretical proposal of high performance blood components biosensor based on defective 1D photonic crystal employing WS_2, MoS_2 and graphene," *Opt. Quantum Electron.*, vol. 53, no. 7, p. 357, Jul. 2021.

[16] Z. Vafapour et al., "The potential of refractive index nanobiosensing using a multi-band optically tuned perfect light metamaterial absorber," *IEEE Sensors J.*, vol. 21, no. 12, pp. 13786–13793, Jun. 2021.

[17] R. Taubert, M. Hentschel, J. Kästel, and H. Giessen, "Classical analog of electromagnetically induced absorption in plasmonics," *Nano Lett.*, vol. 12, no. 3, pp. 1367–1371, Mar. 2012.

[18] H.-J. Li, L.-L. Wang, and X. Zhai, "Plasmonically induced absorption and transparency based on MIM waveguides with concentric nanorings," *IEEE Photon. Technol. Lett.*, vol. 28, no. 13, pp. 1454–1457, Jul. 1, 2016.

[19] A. Lezama, S. Barreiro, and A. M. Akulshin, "Electromagnetically induced absorption," *Phys. Rev. A, Gen. Phys.*, vol. 59, no. 6, pp. 4732–4735, Jun. 1999.

[20] K. Wen et al., "Single- and dual-plasmonic induced absorption in a subwavelength end-coupled composite-square cavity," *Appl. Opt.*, vol. 56, no. 30, p. 8372, 2017.

[21] M. Cao, T. Wang, H. Zhang, and Y. Zhang, "Tunable electromagnetically induced absorption based on graphene," *Opt. Commun.*, vol. 413, pp. 73–79, Apr. 2018.

[22] Y. Neo, T. Matsumoto, T. Watanabe, M. Tomita, and H. Mimura, "Transformation from plasmon-induced transparence to -induced absorption through the control of coupling strength in metal-insulator-metal structure," *Opt. Exp.*, vol. 24, no. 23, p. 26201, 2016.

[23] A. W. Brown and M. Xiao, "All-optical switching and routing based on an electromagnetically induced absorption grating," *Opt. Lett.*, vol. 30, no. 7, pp. 699–701, 2005.

[24] D. Floess et al., "Plasmonic analog of electromagnetically induced absorption leads to giant thin film Faraday rotation of 14°," *Phys. Rev. X*, vol. 7, no. 2, Jun. 2017, Art. no. 021048.

[25] S. K. Chamoli, S. C. Singh, and C. Guo, "Design of extremely sensitive refractive index sensors in infrared for blood glucose detection," *IEEE Sensors J.*, vol. 20, no. 9, pp. 4628–4634, May 2020.

[26] S. Ghorbani, M. Sadeghi, and Z. Adelpour, "A highly sensitive and compact plasmonic ring nano-biosensor for monitoring glucose concentration," *Laser Phys.*, vol. 30, no. 2, Feb. 2020, Art. no. 026204.

[27] Z. A. Zaky, A. M. Ahmed, A. S. Shalaby, and A. H. Aly, "Refractive index gas sensor based on the Tamm state in a one-dimensional photonic crystal: Theoretical optimisation," *Sci. Rep.*, vol. 10, no. 1, p. 973, Jun. 2020.

[28] B.-F. Wan, Q.-Y. Wang, H.-M. Peng, H.-N. Ye, and H.-F. Zhang, "A late-model optical biochemical sensor based on OTS for methane gas and glucose solution concentration detection," *IEEE Sensors J.*, vol. 21, no. 19, pp. 21465–21472, Oct. 2021.

[29] M.-L. Wan, J.-N. He, Y.-L. Song, and F.-Q. Zhou, "Electromagnetically induced transparency and absorption in plasmonic metasurfaces based on near-field coupling," *Phys. Lett. A*, vol. 379, nos. 30–31, pp. 1791–1795, Sep. 2015.

Bao-Fei Wan was born in Jiangsu, China, in 1997. He is currently pursuing the master's degree with the College of Electronic and Optical Engineering and the College of Flexible Electronics (Future Technology), Nanjing University of Posts and Telecommunications, Nanjing, China.

His main research interests involve optical sensors, nonreciprocal devices, and angular selection structures.

Bing-Xiang Li received the Ph.D. degree in chemical physics from the Advanced Materials and Liquid Crystal Institute, Kent State University, Kent, OH, USA, in 2019.

He is currently a Professor with the College of Electronic and Optical Engineering and the College of Flexible Electronics (Future Technology), Nanjing University of Posts and Telecommunications, Nanjing, China. His research interests include metamaterials, liquid crystals, stimuli-responsive soft materials, nonequilibrium systems, active matter, and biophysics.

Hai-Feng Zhang received the Ph.D. degree from the College of Electronic and Information Engineering, Nanjing University of Aeronautics and Astronautics, Nanjing, China, in 2014.

He is currently working as a Professor with the College of Electronic and Optical Engineering and the College of Flexible Electronics (Future Technology), Nanjing University of Posts and Telecommunications, Nanjing. His main research interests include computational electromagnetics, plasma photonic crystal, plasma stealthy, and electromagnetic properties of metamaterials.